MOLECULAR PHYSICS
2020, VOL. 118, NO. 6, e1644384 (18 pages)
https://doi.org/10.1080/00268976.2019.1644384

Taylor & Francis
Taylor & Francis Group

RESEARCH ARTICLE

Intrinsically smooth discretisation of Connolly's solvent-excluded molecular surface

Adrian W. Lange*, John M. Herbert, Benjamin J. Albrecht† and Zhi-Qiang You‡

Department of Chemistry and Biochemistry, The Ohio State University, Columbus, OH, USA

ABSTRACT

The switching/Gaussia (SWIG) algorithm for intrinsically smooth discretisation of the van der Waals cavity surface, for use in implicit solvation modelling, is extended here to the case of the solvent-excluded surface (SES), also known as the Connolly surface or sometimes the molecular surface. In conjunction with a polarisable continuum model (PCM), SES-SWIG discretisation affords continuum electrostatics that vary smoothly with respect to the nuclear coordinates, with a solvation energy that is analytically differentiable with respect to those coordinates. If the SES is the desired cavity construction, then the PCM + SES-SWIG method represents an efficient, boundary-element alternative to three-dimensional, finite-difference solution of Poisson's equation. The algorithm introduced here allows the SES to be constructed and discretised quickly and easily, and its analytically differentiable form paves the way for derivation of analytic gradients.

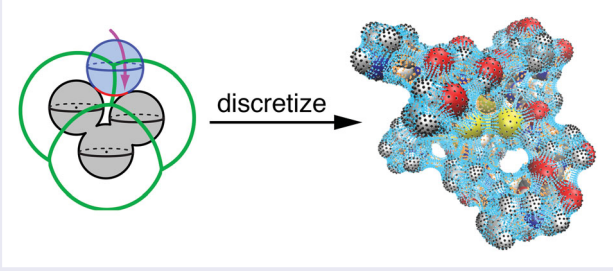

ARTICLE HISTORY
Received 1 June 2019
Accepted 10 July 2019

KEYWORDS
Molecular surface; polarisable continuum; implicit solvent

I. Introduction

The electrostatic interaction between an arbitrary charge distribution (solute) and a dielectric continuum (solvent) is defined by the solution to Poisson's equation. That equation, however, does not specify how to determine the boundary between the solute and the continuum, which is a crucial aspect of any implicit solvation model. Various definitions of this 'solute cavity' are in common use, most based at some level on a union of atom-centred spheres. While atomic van der Waals (vdW) radii are available from crystallographic data [1,2], a solvent molecule is prevented by its own finite size from approaching so close to the solute. Thus, crystallographic vdW radii are often scaled by a factor greater than unity (typically 1.2) for use in continuum electrostatics calculations [3–5].

Alternatively, one may augment the atomic vdW radii by an additional 'solvent probe' radius, r_{probe}, representing the approximate size of a solvent molecule, e.g. $r_{\text{probe}} = 1.4$Å for water. (This represents half the distance to the first peak in the oxygen–oxygen radial distribution function of the neat solvent [6].) This definition,

$$r_{\text{SAS}} = r_{\text{vdW}} + r_{\text{probe}}, \tag{1}$$

results in what is usually called the *solvent-accessible surface* (SAS). An example of the SAS and its relationship to the vdW surface is illustrated in Figure 1. As suggested in the figure, the SAS may be conceptualised as the locus of centre points of a spherical solvent probe, whose radius is r_{probe}, as that probe rolls over the vdW

CONTACT John M. Herbert herbert@chemistry.ohio-state.edu Department of Chemistry and Biochemistry, The Ohio State University, Columbus, OH 43210, USA
*Present address: Tempus, Chicago, IL, USA
†Present address: Cray Inc., Seattle, WA, USA
‡Present address: Ohio Supercomputer Center, Columbus, OH, USA

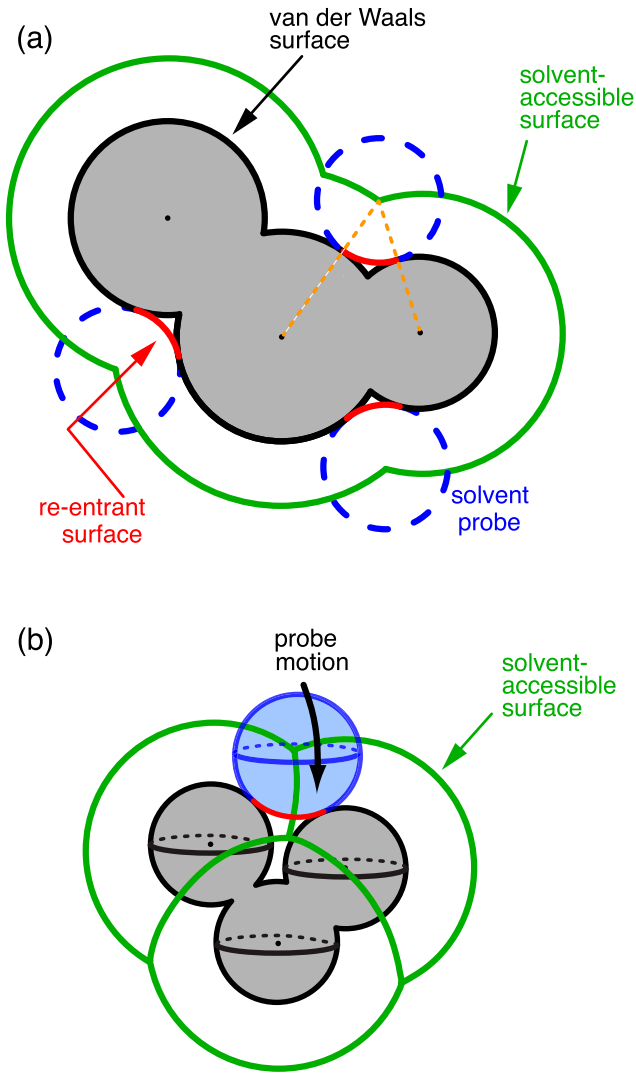

Figure 1. (a) Two-dimensional and (b) three-dimensional depictions of how a spherical solvent probe is used to define various cavity surfaces. The van der Waals (vdW) surface and the solvent-accessible surface (SAS) are defined in the same way but using different radii for the atom-centred spheres (see Equation (1)). Alternatively, the SAS can be viewed as the locus of centre points of a spherical solvent probe (the blue circle) as it rolls over the vdW surface. The solvent-excluded or Connolly surface (SES) is not shown in its entirety, but smooths out the cusps in the vdW surface by adding the 're-entrant' surfaces (indicated in red), in cases where the probe sphere is simultaneously in contact with more than one atom-centred sphere. These re-entrant surfaces, along with the 'contact surface' between the vdW surface and the solvent probe, together define the SES. In (a), the two broken line segments shown in orange subtend the re-entrant surface element shown in red, and thereby demonstrate how projection of discretisation points from the SAS back onto the vdW surface automatically eliminates points on the vdW surface that ought to be replaced with points on the re-entrant surfaces when the SES is constructed.

surface. The SAS is sometimes called the *Lee-Richards surface*, after the authors who first proposed it as a measure of solvent accessibility in proteins [7], but we shall not use that terminology here. There exists some ambiguity about terminology in the literature [8,9], with what we call the SES sometimes being called the SAS; see Ref. [10] for a recent example. We follow the convention of Ref. [11], which is consistent with the terminology used in the context of polarisable continuum models (PCMs) [12].

Both the SAS and the vdW surface exhibit cusps along the seams of intersection between atomic spheres. These may prove numerically problematic for implicit solvent models that depend upon the electric field normal to the cavity surface [12–15], since the surface normal is discontinuous at the cusps. Moreover, for macromolecular solutes these cusps lead to high-dielectric crevices buried in the interior of the solute [16–20].

To remove the cusps, Richards [21] suggested combining the *contact surface* (defined by the points of contact between the solvent probe and the SAS) with the *re-entrant surfaces* (defined as the inward-facing surface of the probe, in cases where the probe makes simultaneous contact with more than one atom-centred sphere). Together, the contact and re-entrant surfaces constitute what we will call the *solvent-excluded surface* (SES), although Richards originally called it the *molecular surface* [21], a term that is still sometimes used synonymously with SES. Also synonymous is the term *Connolly surface*, in acknowledgement of the fact that it was Connolly who popularised this particular surface construction [22], and who also developed the first analytic algorithm for constructing it [23]. Alternative algorithms for constructing the SES were developed subsequently [8,10,24–46], mostly in the interest of fast rendering and visualisation of the SES for large molecules and/or computing molecular surface areas.

The SES enjoys a long history in the context of molecular visualisation [11,22,42,45,47], and is sometimes used in scoring functions for molecular docking [48,49], and also increasingly in the context of continuum electrostatics, specifically finite-difference Poisson-Boltzmann calculations [16,19,36,50–52]. The latter are always subject to numerical discontinuities that must be fought against by means of interpolation and dense grids [53–56], and the SES has proven particularly problematic in this respect [57,58]. In the context of generalised Born models [59], which are the most popular implicit solvation models in biomolecular simulations, an analytic alternative to the original SES was developed [58,60,61], known as the *generalised Born molecular volume* (GBMV) model [58]. This algorithm uses a switching function to smooth out the aforementioned cusps, providing molecular surface areas that are good approximations to those obtained using the SES.

Discontinuities as the atomic coordinates are displaced are also a problem in boundary-element approaches to continuum electrostatics [62–67], unless specific efforts are taken to eliminate them. This is true even if the mathematical specification of the surface is smooth, and indeed Figure 1 correctly suggests that the analytic SES is smooth, in the sense that its first derivatives are continuous functions. However, numerical continuum electrostatics calculations require discretisation of the surface, and discontinuities arise because the number of discretisation points is not fixed. Atomic motions expose, or alternatively bury, parts of the cavity surface.

Here, we introduce an intrinsically smooth numerical discretisation algorithm that can be used for explicit construction of the SES for use in continuum electrostatics calculations. This algorithm combines Connolly's prescription [23] for constructing the SES with an algorithm for smooth discretisation of the SAS or the vdW surface. The latter was developed previously by Lange and Herbert [66–69], as a generalisation of earlier smooth cavity discretisation schemes [62,63], and has seen extensive use in conjunction with PCMs [5,12,13,15,70,71]. These are are a particular class of boundary-element dielectric continuum models that, in the case of a classical solute whose charge distribution is entirely contained within the solute cavity, provide an exact solution for the continuum electrostatic solvation energy, equivalent to what would be obtained from the electrostatic potential that comes from solving Poisson's equation [5,14]. For a quantum-mechanical solute, where the tails of the wave function penetrate into the dielectric medium, the associated 'volume polarisation' can be treated approximately [14,15]. Of particular relevance is recent work suggesting that use of the SES may help to avoid undesirable artifacts in PCM calculations that include explicit solvent molecules [72,73]. As such, we wish not only to *construct* the SES (analytic equations for which were written down long ago by Connolly [23]) but also to *discretise* it, for use in a PCM.

Our surface discretisation algorithm [66,67] uses systematically-improvable, atom-centred Lebedev quadrature grids [74,75]. Grid points are therefore assignable to nuclei so there is no ambiguity regarding how to associate the forces that are generated by changes in the dielectric boundary to individual atoms, as there is for grid-based Poisson solvers [76]. A switching function is used to smoothly attenuate the contribution from each grid point as it passes into the interior of the solute cavity, thus guaranteeing a potential energy surface that is a continuous function of the atomic coordinates. However, use of a switching function has the unintended consequence of allowing discretisation points to approach one another more closely than they would if they were discarded abruptly upon entering the cavity interior. Because the Coulomb self-energy of the cavity surface charge is required in order to solve the PCM equations, the close approach of surface discretisation points causes undesirable oscillations in the solvation energy and its gradient as the atoms are displaced [66]. These unwanted oscillations can be eliminated if the point charges q_i, which are located at the surface discretisation points $\mathbf{s}_i$ and represent the surface charge induced by polarisation of the continuum, are replaced by Gaussian functions:

$$g_i(\mathbf{r}) = q_i(\zeta_i^2/\pi)^{3/2} \exp(-\zeta_i^2|\mathbf{r} - \mathbf{s}_i|^2). \qquad (2)$$

This was originally suggested by York and Karplus [62]. The Coulomb interaction of two Gaussian-blurred charges remains finite even as the distance between their centres goes to zero. This modification, along with the use of a switching function and Lebedev grids, defines what we call the 'switching/Gaussian' (SWIG) discretisation procedure [66,67].

Previously, we implemented the SWIG algorithm only for cavity surfaces constructed from atom-centred spheres, i.e. the vdW surface or SAS [66–68]. Here, we extend this procedure to discretisation of the SES. This proves to be considerably more involved, as Connolly's algorithm for constructing the SES uses not only atom-centred spheres (for the contact surface) but also additional spheres and tori for the re-entrant surfaces. The result is a discretised form of the SES that is intrinsically smooth with respect to displacement of the atomic coordinates, and numerical examples will demonstrate that smooth potential energy surfaces for the solute are indeed obtained. In principle, the SES construction reported here is amenable to analytic energy gradients that should provide smooth forces for stable molecular dynamics simulations in implicit solvent, although we have not yet implemented the gradients. Even so, the SES construction provided here is useful for benchmark purposes and we have already used it in this capacity in two papers concerning generalised Born models [77,78], although details of the surface construction were not provided in those papers.

II. Overview of the algorithm

We first provide an overview of the analytic SES and an outline of our algorithm for discretising it. The detailed mathematics is relegated to Section III. To the extent possible, we follow the the terminology and notation in Connolly's work [23]. A notable exception is that we will use capital letters $I, J, K, \ldots$ for atomic indices, whereas lower-case letters $i, j, k, \ldots$ will index grid points.

A. Nature of the analytic SES

In three dimensions, construction of the SES is more complicated than the two-dimensional example in Figure 1(a) suggests, and consists of the contact surface and two types of re-entrant surfaces. These three types of surface facets arise from cases where the spherical solvent probe is tangent to only a single atomic sphere (which therefore retains two degrees of freedom), cases where the probe touches two atomic spheres simultaneously (where only one degree of freedom remains), and cases where the probe is simultaneously in contact with three atomic spheres (with no remaining degrees of freedom). Cases where the probe sphere has zero, one, or two degrees of freedom lead to the following three types of surface elements.

- *Two degrees of freedom*. Convex portions of atom-centred spheres, representing the two-dimensional contact surface.
- *One degree of freedom*. Concave portions of tori, generated by the one-dimensional regions where the probe sphere makes simultaneous contact with two atom-centred spheres. An example of what we will call the *toroidal re-entrant surface* between atomic spheres centred at coordinates $\mathbf{a}_I$ and $\mathbf{a}_J$ is depicted in Figure 2. Motion of the probe sphere (while staying in contact with both spheres, I and J) delineates a tangent circle (or *contact circle* [23]) on either atomic sphere. The toroidal re-entrant surface is the concave surface of the probe that lies between the two contact circles.
- *Zero degrees of freedom*. Concave spherical re-entrant surfaces, corresponding to a portion of the probe sphere delineated by points of simultaneous tangency with three different atom-centred spheres. An example is depicted in Figure 3.

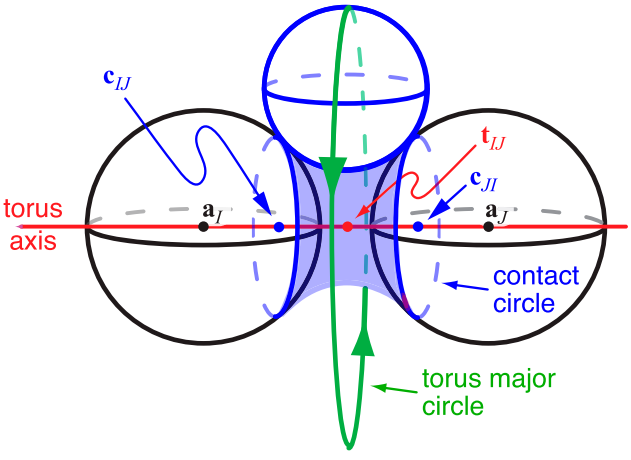

Figure 2. Diagram illustrating construction of the toroidal re-entrant surface between atomic spheres centred at points $\mathbf{a}_I$ and $\mathbf{a}_J$. As the probe sphere (depicted in blue) is rolled around the one-dimensional surface of simultaneous contact with both atomic spheres, its centre traces out the major circle of a torus, which is depicted in green. The shaded blue region lies on the inner face of this torus, between the two seams delineated by the 'contact circles' centred at points $\mathbf{c}_{IJ}$ and $\mathbf{c}_{JI}$. The contact circles represent the points of tangency between the probe sphere and either atomic sphere. This shaded blue region defines the toroidal re-entrant surface.

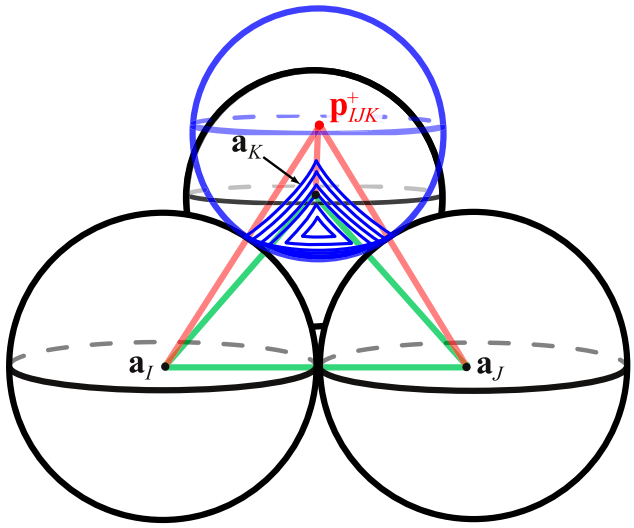

Figure 3. Diagram illustrating construction of a spherical re-entrant surface, contours of which are depicted as curved blue triangles and correspond to a portion of a probe sphere centred at the point $\mathbf{p}^{+}_{IJK}$, which is simultaneously in contact with atomic spheres I, J, and K. The base triangle connecting $\mathbf{a}_I$, $\mathbf{a}_J$, and $\mathbf{a}_K$ is shown in green, and together with the pale red lines makes up a tetrahedron having vertices $\mathbf{a}_I$, $\mathbf{a}_J$, $\mathbf{a}_K$, and $\mathbf{p}^{+}_{IJK}$. For clarity, this diagram omits a second probe sphere that is centred at a point $\mathbf{p}^{-}_{IJK}$ on the opposite side of the base triangle relative to $\mathbf{p}^{+}_{IJK}$. That second probe is used to construct a complementary re-entrant surface on the opposite side of the base triangle. Note that points on the probe circle sphere outside of the tetrahedron are discarded.

Each of these surface facets is considered in turn in Section II B.

Note that Connolly's original implementation of the SES algorithm [47] is susceptible to occasional topological singularities that render it unable to construct the surface [33]. These difficulties are specifically associated with the toroidal re-entrant surface facets, and they are eliminated in our algorithm as discussed in Section II B 2.

B. Algorithm to discretise the SES

The three types of surface facets described above must each be discretised, and we refer to the resulting grids as the atomic grid, the toroidal re-entrant grid, and the spherical re-entrant grid, respectively. Each is a piece of the final, discretised SES, involving one, two, or three

atoms, respectively. There are three main steps in our algorithm, corresponding to construction of each type of grid. These are discussed one by one in the sections that follow.

1. Atomic grids (Contact surface)

The first step is to compute the SAS, with a probe radius r_{probe}, using the 'improved' SWIG (ISWIG) method [67]. (This method simply replaces the switching function used in our original work [66] with a somewhat different functional form, from Ref. [67].) The SAS consists of atom-centred spheres whose radii are equal to $r_I + r_{\text{probe}}$, where r_I is the vdW radius for atom I. Each sphere is discretised with a Lebedev grid and the ith grid point is subject to the ISWIG switching function F_i^{atomic} that is introduced below. This grid point is discarded if $F_i^{\text{atomic}} < \Theta_{\text{sw}}$, where the dimensionless drop tolerance is set to $\Theta_{\text{sw}} = 10^{-6}$, as in previous work [67]. Grid points that are not discarded are then translated inward along the radial surface normal vectors, by a distance r_{probe}, so that they ultimately reside on the vdW surface.

Formally speaking, discontinuities in the potential surface remain so long as Θ_{sw} is finite, but the same is true, e.g. for shell-pair and integral-screening drop tolerances, and in any case Θ_{sw} is a controllable parameter that can be made as small as machine precision if required. In our experience, setting $\Theta_{\text{sw}} = 10^{-6}$ does not engender any perceptible discontinuities, as our numerical results will confirm.

2. Toroidal re-entrant grids

The next step is to locate the toroidal portions of the re-entrant surface. These connect pairs of atoms I and J whose separation $d_{IJ} = \|\mathbf{a}_I - \mathbf{a}_J\|$ satisfies the criterion

$$d_{IJ} < R_I + R_J \tag{3}$$

where

$$R_I = r_I + r_{\text{probe}} \tag{4}$$

is the augmented SAS radius for atom I. Equation (3) serves as a cutoff distance in a pairwise search. In addition, the search is limited to atoms I and J having at least one remaining grid point following construction of the atomic grids and application of the switching function F_i^{atomic}. (Otherwise, the atom in question does not contribute to the SAS and therefore cannot support a toroidal re-entrant surface.) This significantly reduces the search effort in many cases, and excludes nearly all of the interior atoms in large, globular molecules such as the proteins considered in some of our previous work [77,78].

For atom pairs IJ that are not excluded, a toroidal grid connecting the two vdW spheres is constructed, which discretises the translucent blue surface shown in Figure 2. Two switching functions are then applied to grid points on this torus. The first of these eliminates the case of a 'self-intersecting' or 'spindle' torus, in which the distance between the centre of the solvent probe sphere and the centre of the torus ($\mathbf{t}_{IJ}$ in Figure 2) becomes smaller than r_{probe}. (In mathematical language [79,80], this means that the major radius of the torus becomes smaller than its minor radius.) The case of a self-intersecting torus causes instabilities in Connolly's original SES algorithm [33], but these are handled automatically by the algorithm presented here. We have yet to encounter cases where the SES could not be constructed according to the present prescription.

Finally, a second switching function smoothly attenuates grid points outside of the region delineated by the two contact circles. If the solvent probe is able to roll completely around this torus without making contact with a third atomic sphere, then the result is a 'free' torus, to use Connolly's terminology [23]. In this case, the toroidal grid for atom pair (I, J) is then complete.

3. Spherical re-entrant grids

The third type of surface facet is the spherical re-entrant surface. To determine where these are required, we check for three-body contacts by considering the pairwise list of atoms (I, J) for which toroidal re-entrant grids were constructed, then subjecting this list to another switching function that removes grid points on any atom K that is inaccessible to the solvent probe sphere. Any toroidal grid point for which this third switching function is too small ($F_i^{\text{torus}} < \Theta_{\text{sw}}$) is discarded.

The final step is to create the spherical portions of the re-entrant surfaces wherever three-body contacts are found. Such contacts can exist between atoms I, J, and K only if

$$d_{IJ} < R_I + R_J \tag{5a}$$

$$d_{IK} < R_I + R_K \tag{5b}$$

$$d_{JK} < R_J + R_K. \tag{5c}$$

Rather than performing a cubic-scaling search over triples (I, J, K), we leverage information from the previously-determined tori to limit the search to unique pairs (I, J) that are connected by a toroidal re-entrant surface, and for those atoms K for which either (I, K) or (J, K) is also connected by a toroidal re-entrant surface. Having located a satisfactory triple (I, J, K) from the pairwise toroidal list, the distance criteria in Equation (5) are then checked.

For triples (I, J, K) satisfying Equation (5), we compute $\mathbf{p}_{IJK}^{+}$ and $\mathbf{p}_{IJK}^{-}$, which are the centres of the probe sphere when it makes simultaneous contact with spheres I, J, and K. (One of the points $\mathbf{p}_{IJK}^{\pm}$ is centred above the

plane defined by the atomic centres $\mathbf{a}_I$, $\mathbf{a}_J$, and $\mathbf{a}_K$ while the other is positioned below; see Figure 3.) The probe spheres centred at $\mathbf{p}_{IJK}^{\pm}$ are each discretised with a Lebedev grid and several switching functions are applied. One of these accounts for the case in which the probe makes contact with a fourth atom and another accounts for the case where the two probe spheres intersect. Additional switching functions serve to remove grid points exterior to two tetrahedra having vertices at $\mathbf{a}_I$, $\mathbf{a}_J$, $\mathbf{a}_K$, and $\mathbf{p}_{IJK}^{\pm}$, one of which is depicted in Figure 3. Any grid point for which $F_i^{\text{sphere}} < \Theta_{\text{sw}}$ is discarded.

4. Example

Mathematical details of the implementation are provided in Section III, but we first pause to consider an example. Figure 4 depicts the discretised SES generated by our algorithm, for the 384-atom protein 2MRB. (Relative to the structure obtained from the protein data bank, we have removed three Cd^{2+} ions and added missing hydrogens.) Using 110 Lebedev grid points to discretises each atomic sphere, a 20×20 toroidal grid (see Section III D), and a drop tolerance $\Theta_{\text{sw}} = 10^{-6}$, the contact surface consists of 6,537 points while the toroidal and spherical facets of the re-entrant surface consist of 39,922 and 9,271 discretisation points, respectively. Nevertheless, we are able to construct the entire discretisation grid in 11 sec on a single processor. For comparison, using a recently-introduced numerical algorithm for integrating the SES, in the context of finite-difference Poisson-Boltzmann calculations, a timing of 53 sec is reported for 'probe generation' [51].

III. Implementation

This section provides a detailed description of how we implement and discretise Connolly's analytic construction of the SES. Relevant geometrical definitions and equations from Connolly's work [23] are listed in Table 1.

Table 1. Definitions and notation used in the analytic construction of the solvent-excluded surface.[a]

Quantity	Notation and/or definition
Atomic coordinates	$\mathbf{a}_I, \mathbf{a}_J, \mathbf{a}_K, \ldots$
Atomic vdW radii	$r_I, r_J, r_K, \ldots$
Probe radius	r_{probe}
Atomic SAS radius	$R_I = r_I + r_{\text{probe}}$
Interatomic distance	$d_{IJ} = \|\mathbf{a}_I - \mathbf{a}_J\|$
Torus axis unit vector	$\mathbf{u}_{IJ} = (\mathbf{a}_I - \mathbf{a}_J)/d_{IJ}$
Torus centre	$\mathbf{t}_{IJ} = \frac{1}{2}(\mathbf{a}_I + \mathbf{a}_J) + \frac{1}{2}(\mathbf{a}_J - \mathbf{a}_I)(R_I^2 - R_J^2)/d_{IJ}^2$
Torus radius	$r_{IJ} = \frac{1}{2}[(R_I + R_J)^2 - d_{IJ}^2]^{1/2}[d_{IJ}^2 - (r_I - r_J)^2]^{1/2}/d_{IJ}$
Contact circle centre	$\mathbf{c}_{IJ} = (r_I \mathbf{t}_{IJ} + \mathbf{a}_I r_{\text{probe}})/R_I$
Base triangle angle	$\omega_{IJK} = \cos^{-1}(\mathbf{u}_{IJ} \cdot \mathbf{u}_{IK})$
Base plane normal vector	$\mathbf{u}_{IJK} = (\mathbf{u}_{IJ} \times \mathbf{u}_{IK})/\sin(\omega_{IJK})$
Torus base-point unit vector	$\mathbf{u}_{\text{TB}} = \mathbf{u}_{IJK} \times \mathbf{u}_{IJ}$
Base point	$\mathbf{b}_{IJK} = \mathbf{t}_{IJ} + [\mathbf{u}_{IK} \cdot (\mathbf{t}_{IK} - \mathbf{t}_{IJ})]\mathbf{u}_{\text{TB}}/\sin(\omega_{IJK})$
Probe height	$h_{IJK} = (R_I^2 - \|\mathbf{b}_{IJK} - \mathbf{a}_I\|^2)^{1/2}$
Probe position, 3-body contacts	$\mathbf{p}_{IJK}^{\pm} = \mathbf{b}_{IJK} \pm h_{IJK}\, \mathbf{u}_{IJK}$
Vertex	$\mathbf{v}_I = (r_I \mathbf{p}_{IJK} + \mathbf{a}_I r_{\text{probe}})/R_I$

[a]Notation mostly follows that introduced by Connolly in Ref. [23].

A. Atomic grids

The contact surface is formed from atomic grids that are constructed by first building a SAS and then projecting the grid points back onto the vdW surface, along the surface normals. The discretised SAS consists of a Lebedev grid of radius $r_I + r_{\text{probe}}$ centred at the point $\mathbf{a}_I$, for each atom I. The atomic switching function

$$F_i^{\text{atomic}} = \prod_{J, i \notin J}^{\text{atoms}} f_i^J \tag{6}$$

for the grid point $i \in I$ is a slightly modified version of the ISWIG switching function [67]. It is a product of 'primitive' switching functions, one for each atom $J \neq I$:

$$f_i^J = 1 - \tfrac{1}{2}\{\text{erf}[\gamma_i^{\text{atomic}}(R_J - d_{iJ})] + \text{erf}[\gamma_i^{\text{atomic}}(R_J + d_{iJ})]\}. \tag{7}$$

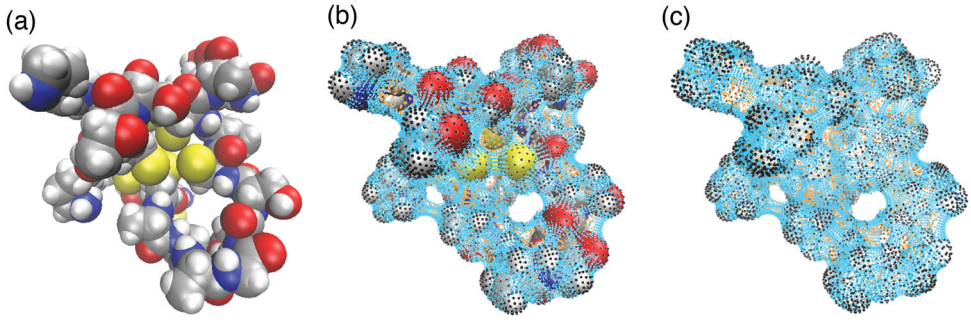

Figure 4. Examples of the discretised SES for a small protein (PDB code 2MRB, 384 atoms). Depicted are (a) a model of the protein based on van der Waals atomic spheres, (b) the discretised SES superimposed upon the van der Waals spheres, and (c) the discretised SES alone. Discretisation points for the atomic contact surfaces are shown in black, those for the toroidal facets of the re-entrant surfaces in cyan, and those for the spherical facets of the re-entrant surfaces in orange.

Here, $d_{iJ} = \|\mathbf{s}_i - \mathbf{a}_J\|$ is the distance between the surface discretisation point $\mathbf{s}_i$ and the atomic centre (nucleus) located at $\mathbf{a}_I$. The function f_i^J contains a parameter

$$\gamma_i^{\text{atomic}} = \frac{\zeta^{\text{atomic}}}{w_i^{1/2} R_I} \tag{8}$$

where w_i is the Lebedev quadrature weight associated with the point $\mathbf{s}_i$. The parameter ζ^{atomic} plays the role of the Gaussian width parameter ζ in Equation (2). (We call it ζ^{atomic} because a different width parameter, ζ^{torus}, will be used in discretising the toroidal portions of the surface.) As in our previous work on SWIG discretisation [66,67], we take the value of ζ^{atomic} from Ref. [81], in which a different value of ζ is optimised for each different Lebedev grid in order to reproduce the energy for the Born ion model of a point charge centred in a spherical cavity inside of a continuum dielectric medium. In other words, once the number of Lebedev grid points per atomic sphere has been selected, which determines the quality of the discretisation, then ζ^{atomic} can be obtained from the values tabulated in Ref. [81].

After F_i^{atomic} is evaluated for each grid point and the grid pruned accordingly (using the drop tolerance Θ_{sw}), these SAS surface points are projected back along the outward-pointing surface normal vectors $\mathbf{n}_i$, each by a distance r_{probe}, so that they lie on the vdW surface:

$$\mathbf{s}_i^{\text{atomic}} = \mathbf{s}_i^{\text{SAS}} - r_{\text{probe}} \mathbf{n}_i. \tag{9}$$

As shown in Figure 1(a), this backwards projection automatically eliminates that portion of the vdW surface that is to be replaced by a re-entrant surface.

The surface area associated with the ith grid point, assuming that it resides on a sphere of radius η_I, is [66]

$$\tilde{a}_i^{\text{atomic}} = w_i \eta_I^2. \tag{10}$$

To ensure that the surface area is a smooth function of the atomic coordinates, these areas must be scaled by the switching function. We therefore define the surface area associated with grid point $\mathbf{s}_i$ to be [66]

$$a_i^{\text{atomic}} = \tilde{a}_i^{\text{atomic}} F_i^{\text{atomic}}. \tag{11}$$

The total surface area of the contact portion of the SES is then the sum of all a_i^{atomic}. Similarly, if we define

$$a_i^{\text{SAS}} = w_i R_I^2 F_i^{\text{atomic}}, \tag{12}$$

then the sum over all i in Equation (12) affords the total surface area of the SAS.

B. Toroidal re-entrant grids

If the torus axis in Figure 2 is taken to be the z axis, then the torus suggested in the figure is defined by the equation [79]

$$\left(r_{IJ} - \sqrt{x^2 + y^2}\right)^2 + z^2 = r_{\text{probe}}^2, \tag{13}$$

or else parametrically as [79]

$$x = (r_{IJ} + r_{\text{probe}} \cos\theta) \cos\phi \tag{14a}$$

$$y = (r_{IJ} + r_{\text{probe}} \cos\theta) \sin\phi \tag{14b}$$

$$z = r_{\text{probe}} \sin\theta \tag{14c}$$

for $\theta, \phi \in [0, 2\pi)$. The quantities r_{IJ} (Table 1) and r_{probe} are the major and minor radii of the torus, respectively. Examples are shown in Figure 5.

To construct the toroidal grids, we first create a primitive toroidal grid by discretising a torus as a 'circle of circles' around the torus axis in Figure 2; see also Figure 5. The minor circle of the torus has radius r_{probe}, and a minor circle grid is divided into N_1 points of equal arc length, $\Delta\theta_1 = 2\pi/N_1$. Likewise, a major circle is divided into N_2 parts of equal arc length, $\Delta\theta_2 = 2\pi/N_2$. (In practice, we will set $N_1 = N_2$, but this is not required.) The major circle radius will ultimately be set equal to the torus radius, r_{IJ}. A set of N_2 radial unit vectors lying in the

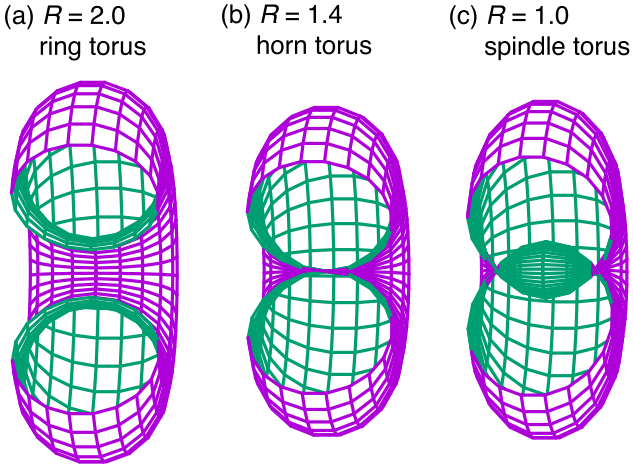

Figure 5. Cutaway cross sections of various tori, each with a minor (tube) radius of $r = 1.4$ (in arbitrary units) but having different values for the major (wheel) radius, R, as indicated. (a) The 'ring' torus (or 'free' torus, in Connolly's language [23]) is characterised by $R > r$ and is the case depicted also in Figure 2. (b) The 'horn' torus is the special case where $R = r$. (c) For $R < r$, one obtains a 'self-intersecting' or 'spindle' torus, containing an inner (spindle) surface that is sometimes called the 'lemon surface' [79]. Both the horn and spindle tori lack the familiar 'doughnut hole' of the ring torus, but the horn can nevertheless be discretised in the same manner as the ring.

plane perpendicular to the unit axis are then computed, each pointing from the origin outward with the arc length spacing $\Delta\theta_2$. The surface normals of the primitive torus are computed initially here, pointing outward from the minor circle centres.

As discussed in Section II B, a toroidal re-entrant surface will only exist between two atoms for which $d_{IJ} < R_I + R_J$, and only if atoms I and J each possess at least one non-negligible atomic surface grid point. Additionally, we check the sign of the two radicands in the definition of r_{IJ} (see Table 1), and if either is negative then the candidate torus is discarded. We perform a pairwise atom search with these screening criteria, in order to find atom pairs that will support a toroidal re-entrant surface. Having located such a pair (I, J), the primitive toroidal grid described above is translated to the torus centre, $\mathbf{t}_{IJ}$, and rotated such that the primitive torus axis aligns with $\mathbf{u}_{IJ} = (\mathbf{a}_I - \mathbf{a}_J)/d_{IJ}$. The minor circle grids are then translated outward along the rotated radial vectors by a distance r_{IJ}, forming the complete toroidal grid connecting atomic spheres I and J. At this stage we also compute the surface normal vectors $\mathbf{n}_i^{\text{torus}}$, for the torus in its final position and orientation.

A switching function

$$F_i^{\text{torus}} = g_{i,1}^{IJ} g_{i,1}^{JI} g_{i,2} g_{i,3} \tag{15}$$

for the toroidal grid points is itself a product of four primitive switching functions. The functions $g_{i,1}^{IJ}$ and $g_{i,1}^{JI}$ measure the extent to which the ith grid point lies beyond the plane of the contact circle centre, $\mathbf{c}_{IJ}$, on both sides of the torus spanning atoms I and J. In principle, all toroidal grid points should lie *between* the planes defined by the two contact circles (see Figure 2), but in the spirit of the SWIG method they are allowed to penetrate slightly beyond that plane, so that they may be smoothly attenuated to zero weight. This is accomplished via the switching function

$$g_{i,1}^{IJ} = \tfrac{1}{2}\left[1 + \text{erfc}(2\zeta^{\text{torus}} c_{i,IJ})\right], \tag{16}$$

where $c_{i,IJ}$ is the projection of the torus axis $\mathbf{u}_{IJ}$ onto the vector that connects the grid point $\mathbf{s}_i$ to the centre of the contact circle, $\mathbf{c}_{IJ}$:

$$c_{i,IJ} = (\mathbf{s}_i - \mathbf{c}_{IJ}) \cdot \mathbf{u}_{IJ}. \tag{17}$$

Then, for the opposite side of the torus, we have

$$g_{i,1}^{JI} = \tfrac{1}{2}\left[1 + \text{erfc}(2\zeta^{\text{torus}} c_{i,JI})\right] \tag{18}$$

where $c_{i,JI} = -c_{i,IJ}$.

The function $g_{i,2}$ in Equation (15) accounts for the case of a spindle torus [79,80], for which $r_{IJ} < r_{\text{probe}}$. In this case, which is depicted in Figure 5(c), the torus exhibits an inner 'lemon' surface [79], and as the probe sphere rolls over the vdW surface only the lower half of the lemon should be included in the SES. These points are easily identifiable, for if we take the torus axis to be z, then the two halves of a cross section of the lemon in the xz plane are [79]

$$z_{\pm} = \pm\left[(r_{IJ} + r_{\text{probe}})^2 - (x + r_{IJ} - r_{\text{probe}})^2\right]^{1/2}. \tag{19}$$

The intersecting points are removed via the function

$$g_{i,2} = \begin{cases} 1 - \exp\left[-(\zeta^{\text{torus}} d_i^{\text{torus}})^2\right], \\ \quad \text{for } \mathbf{s}_i \text{ on the lower half of the lemon} \\ 0, \\ \quad \text{for } \mathbf{s}_i \text{ on the upper half of the lemon} \end{cases}. \tag{20}$$

Here, d_i^{torus} is the distance from the ith toroidal grid point $\mathbf{s}_i$ to the torus axis $\mathbf{u}_{IJ}$. The parameter ζ^{torus} is analogous to the parameter ζ^{atomic} for the atomic grid (see Equation (8)), and we have determined a set of values for ζ^{torus}, one for each Lebedev grid density, as described in Section III D. In practice, to determine whether $\mathbf{s}_i$ lies on the appropriate half of the lemon, we compute the distance from the ith grid point to the major circle on the opposite side of the torus. If that distance is less than r_{probe}, then $\mathbf{s}_i$ lies on the wrong half and is discarded.

Finally, the function $g_{i,3}$ in Equation (15) accounts for the possibility of a third atom, K (distinct from I and J) being close enough to the torus that it ought to prevent access by the probe sphere. We use a switching function similar to that used in the ISWIG method [67] to attenuate such points:

$$g_{i,3} = \prod_{K \notin \{I,J\}}^{\text{atoms}} \left[1 + \text{erf}(\zeta^{\text{torus}} \|\mathbf{r}_{ic} - \mathbf{a}_K\|)\right]/2. \tag{21}$$

Here, the points $\mathbf{r}_{ic}$ are centre points of N_1 minor circles of the torus. (That is, these points lie in the middle of the tube, on the torus' major circle). Specifically, $\mathbf{r}_{ic}$ is the centre point closest to $\mathbf{s}_i$, which lies on the torus itself.

Absent the switching functions, the surface area for the ith toroidal grid point is analogous to the 'primitive' atomic surface area $\tilde{a}_i^{\text{atomic}}$ that is defined in Equation (10), and the primitive toroidal surface area is computed as follows. We first compute the perpendicular distance, d_i^{torus}, from the ith toroidal grid point to the torus axis $\mathbf{u}_{IJ}$. (In practice, and for simplicity, we do this prior to rotating the torus from its temporary alignment with the z axis to align it with $\mathbf{u}_{IJ}$.) Note that the circumference of the circle on the torus surface that passes through $\mathbf{s}_i$ and whose normal aligns with $\mathbf{u}_{IJ}$ is $c_i^{\text{torus}} = 2\pi d_i^{\text{torus}}$. The toroidal grid suggested in Figure 5, which we call a 'circle of circles' (imagining a set of circles with

slightly different radii, displaced along the torus axis) naturally divides the toroidal surface circle into N_2 segments, and the ith grid point owns an arc length equal to c_i^{torus}/N_2. Analogously, the minor circle has been divided into N_1 portions, and the ith grid point owns an arc whose length is $2\pi r_{\text{probe}}/N_1$. Taken together, this affords a primitive surface area

$$\tilde{a}_i^{\text{torus}} = \frac{4\pi^2 r_{\text{probe}} d_i^{\text{torus}}}{N_1 N_2} \tag{22}$$

for the ith toroidal grid point.

The analytic result for the surface area of a torus is $4\pi^2 Rr$, where $R = r_{IJ} + r_{\text{probe}}$ is the radius of the major circle of the torus and $r = r_{IJ} - r_{\text{probe}}$ is the radius of its minor circle. Summing Equation (22) over i reproduces this result to high accuracy for any of the torus grids that we have investigated having $N_1 \geq 6$ and $N_2 \geq 6$. Applying the toroidal switching functions for smoothness, the actual contribution to the SES surface area that arises from the toroidal grid point $\mathbf{s}_i$ is

$$a_i^{\text{torus}} = \tilde{a}_i^{\text{torus}} F_i^{\text{torus}} \tag{23}$$

analogous to Equation (11) for a_i^{atomic}.

C. Spherical re-entrant grids

As discussed in Section II B, candidate triples of atoms (I, J, K) are selected by searching those pairs of atoms that are already known to be connected by a toroidal grid. If I and J are connected by a toroidal grid, and if either I and K, or else J and K, are also connected by a toroidal grid, then (I, J, K) may involve a three-body contact with the probe sphere. This will be the case if all three distance criteria in Equation (5) are satisfied, in which case a spherical re-entrant grid is required. Lebedev grids of radius r_{probe} are then centred at the two positions $\mathbf{p}_{IJK}^{\pm}$. These two probe spheres lie tangent to all three atoms I, J, and K.

The switching function for the ith spherical re-entrant grid point is a product of elementary switching functions,

$$F_i^{\text{spherical}} = h_{i,1} h_{i,2} h_{i,3} h_{i,4}^{\pm} h_{i,5} \delta_i, \tag{24}$$

which depend on whether $\mathbf{s}_i$ is on the $\mathbf{p}_{IJK}^{+}$ sphere or the $\mathbf{p}_{IJK}^{-}$ sphere. Functions $h_{i,1}$, $h_{i,2}$, and $h_{i,3}$ are used to determine if $\mathbf{s}_i$ lies inside either of the tetrahedra whose triangular bases are formed by the atomic coordinates $\mathbf{a}_I$, $\mathbf{a}_J$, and $\mathbf{a}_K$, and whose peaks are located at $\mathbf{p}_{IJK}^{+}$ and $\mathbf{p}_{IJK}^{-}$; see Figure 3. We will refer to the triangle $\mathbf{a}_I$-$\mathbf{a}_J$-$\mathbf{a}_K$ as the base of the tetrahedron, and the remaining three faces as its sides. Vectors normal to these three sides are

$$\mathbf{n}_1 = \frac{\mathbf{u}_{IJ} \times (\mathbf{p}_{IJK} - \mathbf{a}_I)}{\|\mathbf{u}_{IJ} \times (\mathbf{p}_{IJK} - \mathbf{a}_I)\|} \tag{25a}$$

$$\mathbf{n}_2 = \frac{\mathbf{u}_{IJ} \times (\mathbf{p}_{IJK} - \mathbf{a}_J)}{\|\mathbf{u}_{IJ} \times (\mathbf{p}_{IJK} - \mathbf{a}_J)\|} \tag{25b}$$

$$\mathbf{n}_3 = \frac{(\mathbf{p}_{IJK} - \mathbf{a}_K) \times \mathbf{u}_{IJ}}{\|(\mathbf{p}_{IJK} - \mathbf{a}_K) \times \mathbf{u}_{IJ}\|} \tag{25c}$$

in which $\mathbf{p}_{IJK}$ could be either $\mathbf{p}_{IJK}^{+}$ or $\mathbf{p}_{IJK}^{-}$, depending on which tetrahedron we are considering for the grid point in question.

The three sides of the tetrahedron intersect the probe sphere along its great circles. Using the normal vectors in Equation (25), we can compute the distance between $\mathbf{s}_i$ and the planes that define each of the three sides of the tetrahedron:

$$d_{i\alpha} = \mathbf{n}_\alpha \cdot (\mathbf{p}_{IJK} - \mathbf{s}_i) \tag{26}$$

for $\alpha = 1, 2,$ or 3, and $\mathbf{p}_{IJK} = \mathbf{p}_{IJK}^{+}$ or $\mathbf{p}_{IJK}^{-}$, as appropriate. The first three switching functions $h_{i\alpha}$ in Equation (24) are defined in terms of the distances $d_{i\alpha}$:

$$h_{i,\alpha} = \begin{cases} 0, & \text{for } d_{i\alpha} \leq 0 \\ 1 - \exp[-(\gamma_i^{\text{atomic}} d_{i\alpha})^2], & \text{for } d_{i\alpha} > 0 \end{cases}. \tag{27}$$

In short, $F_i^{\text{spherical}} = 0$ whenever $\mathbf{s}_i$ lies on the exterior side of any one of the three planes that make up the sides of the aforementioned tetrahedron.

The switching function $h_{i,4}^{\pm}$ in Equation (24) accounts for the case where the two probes centred at $\mathbf{p}_{IJK}^{+}$ and $\mathbf{p}_{IJK}^{-}$ intersect one another, in which case grid points lying inside the opposite probe sphere need to be removed. This is accomplished by measuring the distance between $\mathbf{s}_i$ on the 'plus' sphere (centered at $\mathbf{p}_{IJK}^{+}$) to the probe position of the 'minus' sphere ($\mathbf{p}_{IJK}^{-}$),

$$d_{ip}^{+} = \|\mathbf{s}_i - (\mathbf{b}_{IJK} - h_{IJK}\mathbf{u}_{IJK})\|, \tag{28a}$$

and *vice versa* for a point on the minus sphere,

$$d_{ip}^{-} = \|\mathbf{s}_i - (\mathbf{b}_{IJK} + h_{IJK}\mathbf{u}_{IJK})\|. \tag{28b}$$

The relevant switching function is then

$$h_{i,4}^{\pm} = \begin{cases} 0, \\ \quad d_{ip}^{\pm} \leq r_{\text{probe}} \\ 1 - \exp\left\{-[\gamma_i^{\text{spherical}}(d_{iP}^{\pm} - r_{\text{probe}})]^2\right\}, \\ \quad d_{ip}^{\pm} > r_{\text{probe}} \end{cases} \tag{29}$$

with

$$\gamma_i^{\text{spherical}} = \frac{\zeta^{\text{atomic}}}{w_i^{1/2} r_{\text{probe}}}. \tag{30}$$

The function $h_{i,5}$ in Equation (24) checks for collisions of the probe sphere with a fourth atom, L, removing grid

points when such a collision occurs. Defining

$$r_{pL} = \|\mathbf{p}_{IJK} - \mathbf{a}_L\| - R_L, \tag{31}$$

this switching function is defined as

$$h_{i,5} = \begin{cases} 1, & r_{pL} \geq 0 \\ \prod_{L \notin \{I,J,K\}}^{\text{atoms}} \exp\left[-(3\gamma_i^{\text{spherical}} r_{pL}/4)^2\right], & r_{pL} < 0 \end{cases}. \tag{32}$$

The probe collides with atom L when $r_{pL} < 0$, at which point $h_{i,5}$ attenuates the switching function smoothly to zero. A factor of 3/4 is included in the exponent of Equation (32) in order to provide switching on a reasonable length scale for the spherical re-entrant surface elements, while using ζ^{atomic} to define $\gamma_i^{\text{spherical}}$ in Equation (30). This is an alternative to introducing a new parameter $\zeta^{\text{spherical}}$ to define the exponent.

Finally, the function δ_i in Equation (24) simply determines whether or not $\mathbf{s}_i$ resides on the correct hemisphere of the probe sphere, which is the hemisphere in contact with the atoms I, J, and K. The other hemisphere will not contribute to the surface. The function δ_i is evaluated by computing the distance d_{iB} from the ith grid point to the base triangle of the tetrahedron,

$$d_{iB} = (\mathbf{b}_{IJK} - \mathbf{s}_i) \cdot \left(\frac{\mathbf{b}_{IJK} - \mathbf{p}_{IJK}}{\|\mathbf{b}_{IJK} - \mathbf{p}_{IJK}\|} \right), \tag{33}$$

for $\mathbf{p}_{IJK} = \mathbf{p}_{IJK}^{+}$ or $\mathbf{p}_{IJK} = \mathbf{p}_{IJK}^{-}$, as appropriate. Then

$$\delta_i = \begin{cases} 1, & d_{iB} \leq h_{IJK} \\ 0, & d_{iB} > h_{IJK} \end{cases}. \tag{34}$$

In practice, δ_i is evaluated prior to the other switching functions in order to avoid unnecessary computation.

Surface areas associated with spherical re-entrant grid points are computed in a manner similar to those for the atomic grid points,

$$a_i^{\text{spherical}} = w_i r_I^2 F_i^{\text{spherical}}. \tag{35}$$

The surface normals are simply

$$\mathbf{n}_i^{\text{spherical}} = \frac{\mathbf{p}_{IJK} - \mathbf{s}_i}{\|\mathbf{p}_{IJK} - \mathbf{s}_i\|} \tag{36}$$

for $\mathbf{p}_{IJK} = \mathbf{p}_{IJK}^{+}$ or $\mathbf{p}_{IJK}^{-}$, as appropriate.

D. Numerical fit for the toroidal exponent

The parameter ζ^{torus} in SES-SWIG is important beyond the construction of the geometrical grid because we assume that the Gaussian surface charges $g_i(\mathbf{r})$ that discretise the toroidal grid (Equation (2)) have width parameters

$$\zeta_i^{\text{torus}} = \frac{\zeta^{\text{torus}}}{(\tilde{a}_i^{\text{torus}})^{1/2}}. \tag{37}$$

Thus, ζ^{torus} is a universal parameter for the toroidal grids. In PCM calculations, this parameter appears in both the Coulomb self-energy of the surface charge as well as the Coulomb interaction between the surface charge and the solute's electrostatic potential. It must therefore be determined carefully in order to afford accurate energetics.

The same can be said for the parameter ζ^{atomic} that controls the widths of the Gaussians used in discretising the spherical parts of the SES, and in that case the value of the width parameter was optimised in Ref. [81] to reproduce the energy of a point charge centred in a spherical cavity (Born ion model [82]), in a conductor medium ($\varepsilon = \infty$), with a Gaussian discretisation of the spherical surface and using a Lebedev quadrature grid. We wish to do something similar in order to determine ζ^{torus}, but we are unaware of any simple analytical model for a toroidal cavity shape. Instead, we fit to a model problem consisting of a uniformly charged ring placed inside a toroidal cavity, such that the charged ring coincides with the major circle of the torus. This system is embedded in a conductor dielectric so that the result is independent of ε and the PCM models tested are exact within numerical precision.

The target polarisation energy (i.e. the energy of the reaction field interacting with the ring of charge) for this model problem is computed with the D-PCM approach [5,12,83,84]. D-PCM is the modern nomenclature [12] for the original PCM of Miertuš, Scrocco, and Tomasi [83,84], but is little-used nowadays because it requires explicit evaluation of the surface normal electric field, whereas more recent models require only the electrostatic potential. In this particular case, however, D-PCM has a unique advantage over other models, as explained below.

For these calculations, we use a point-charge discretisation of the surface charge density, as opposed to the spherical Gaussian charge discretisation of SWIG, in order to make the target D-PCM energy independent of any Gaussian exponents. (Recall that Gaussian blurring only becomes important when switching functions are used, which they will not be for these D-PCM calculations.) The utility of the D-PCM approach is that whereas the diagonal (self-interaction) matrix elements in most PCMs involve approximations to the Coulomb integrals within individual surface elements [5], within D-PCM these matrix elements can be computed exactly using a sum rule [85]. (This sum rule is only approximate for arbitrary cavity shapes and sometimes becomes problematic [67,70], but is free of such problems

Table 2. Convergence behaviour for polarisation energies of a charged ring in a torus, embedded in a dielectric medium.[a]

	energy (kcal/mol)		
N_1	D-PCM	C-PCM	error[b]
6	−49.734	−49.777	0.028
8	−49.783	−49.796	0.009
10	−49.795	−49.798	0.007
12	−49.800	−49.799	0.006
14	−49.802	−49.799	0.006
16	−49.804	−49.799	0.006
18	−49.804	−49.799	0.006
20	−49.805	−49.800	0.005

[a]C-PCM energies are for $\zeta^{\text{torus}} = 4.28$ for all values of N_1, and we take $N_2 = N_1$.[b]Difference between the C-PCM value and the converged ($N_1 = 20$) D-PCM value.

for the special case of a toroidal cavity.) Thus, we employ D-PCM with a point charge discretisation and a sum rule for the diagonal elements in the linear equations that define the model, in order to compute a high-accuracy solvation energy for this charged-ring system. In practice, D-PCM energies are not very different from those computed using C-PCM (which does not employ a sum rule), as seen in Table 2.

While one could exhaustively test many combinations of tori and charged rings, we have opted for simplicity by fitting to only one definition of ring and torus that we feel is within the common realm of application for Connolly surfaces. We choose a ring of radius 3Å and having a total charge of $+e$, discretised as 100 separate point charges spaced at uniform angular increments around the ring, each with a charge of $+0.01e$. This ring is then enclosed in a torus whose major circle has a radius of 3Å. The radius of the minor circle is set to the frequently-used choice of 1.4Å, corresponding to r_{probe} for water [12].

Table 2 shows D-PCM and C-PCM energies computed for this model system, corresponding to grids with $N_1 = N_2$. Several values for ζ^{torus} were tested, and we ultimately settled on the (dimensionless) value $\zeta^{\text{torus}} = 4.28$ for all values of N_1, based on calculations using D-PCM. The D-PCM energies converge to the polarisation energy of −49.805 kcal/mol. C-PCM energies using the same value of ζ^{torus} converge to an energy of −49.800 kcal/mol, which is a comforting check given the significant differences in the working equations for C-PCM versus D-PCM.

IV. Numerical results

A. Computational details

We have implemented the SES-SWIG discretisation in the Q-Chem software package [86,87], and the method was released with Q-Chem v. 5.0. Within our implementation, the solute can be described either using electronic structure theory ('QM') or else using a molecular mechanics (MM) force field, i.e. atomic point charges, since only the solute's electrostatic potential is required. Our implementation allows for QM/MM/PCM calculations although we focus on QM/PCM calculation in this work. The algorithm has been implemented for use with PCMs including C-PCM, COSMO, IEF-PCM, and SS(V)PE; consult the literature for an explanation of these models [5,15,70]. It has also been integrated for use with 'screened' PCMs appropriate for solvents with non-zero ionic strength [69,88,89], including our Debye–Hückel-like screening model (DESMO) [69]. All calculations performed here are done in water ($\varepsilon = 78.4$ and $r_{\text{probe}} = 1.4$Å), hence we will use C-PCM as it is virtually identical to IEF-PCM in high-dielectric solvents [70], but is less expensive.

All calculations use unscaled Bondi radii for the atomic spheres [1], except that the radius for hydrogen is reduced from 1.2 to 1.1Å, per the recommendation in Ref. [2]. To construct the SAS, the Bondi radii are simply increased by an amount equal to r_{probe}. In principle the SES smoothing procedure can be applied to either set of radii (i.e. vdW radii $\{\eta\}$ or SAS radii $\{R_I = \eta + r_{\text{probe}}\}$), and for comparative purposes we will examine both. Use of η corresponds to the traditional definition of the SES, wherein the probe sphere rolls over the vdW surface as depicted in Figure 1. We expect the results from this approach to be roughly comparable (in magnitude at least) to those based on the vdW cavity construction, as the cavity size is about the same but without the cusps in the SES case. We will also consider a non-traditional SES based on atomic radii $\{r_I\}$. This corresponds to rolling the probe sphere over the SAS, so we expect this construction to be more comparable to SAS-based results rather than those based on the vdW surface. We will refer to these two versions of the SES as 'SES(r_{vdW})' and 'SES($r_{\text{vdW}} + r_{\text{probe}}$)', to distinguish which radii are used.

All cavity surfaces are discretised using the SWIG algorithm as described above and in Ref. [67], except as noted in a few examples where we intentionally turn off the smoothing procedure for the vdW surface construction, for demonstrative purposes. We will call this (undesirable) surface construction the 'fixed' vdW surface, because no switching function is employed. For the fixed surface, Lebedev grid points are discarded abruptly as they enter the interior of the solute cavity. Except where otherwise noted, we use 110 Lebedev points per sphere (prior to discarding negligible ones) for both the contact surface and the spherical re-entrant surface. Prior work on the SWIG-vdW surface construction suggests smooth convergence with respect to the number of Lebedev discretisation grid points, with results for $N = 110$ that are converged to < 1 kcal/mol with respect

to the infinite-grid limit [67,70], with rotational invariance errors < 0.1 kcal/mol [67]. We use $N_1 = 20 = N_2$ points for the other surface elements, which affords converged results according to the data in Table 2. A few additional convergence tests for molecular surface areas are presented below.

B. Energy profiles

Grant *et al.* [90] have argued that the SES has the 'unpleasant characteristic [that] the infinitesimal movement of a single atom can produce large surface changes'. In particular, they argue that a small change might immediately exclude an (implicit) solvent molecule, as depicted in Figure 6(a). From a physical point of view, this seems dubious because the total charge that is contained within the cavity does not change as a function of this deformation and therefore one would not expect any abrupt change in the electrostatic solvation energy. (There is no concept, within implicit solvation, of a discrete solvent molecule being 'squeezed out' of the gap that is depicted in Figure 6.) In fact, with a smooth construction of the SES there is no discontinuity in this case at all, as we now demonstrate.

In Figure 6(b) we show the SES-SWIG discretisation grids for the initial and final geometries of the model problem suggested by Grant *et al.* [90]. Each discretisation grid point $\mathbf{s}_i$ is drawn as a sphere whose diameter is equal to $a_i^{1/2}$, where a_i is the surface area associated with that particular grid point. One may note that the density of grid points for the spherical facets of the re-entrant surfaces appears to be greater than it is for the contact surface or the toroidal surfaces, but the grid points on the latter generally have larger individual surface areas as compared to the spherical re-entrant grid points.

To test the scenario envisioned by Grant *et al.* [90], we continuously displace two atomic centres as suggested by the arrows in Figure 6(b), adjusting the 'gap size' between their centres. A classical point charge is placed at the centre of each atomic sphere and the C-PCM polarisation energy (i.e. the solute/continuum electrostatic interaction) is plotted in Figure 7. Both the C-PCM polarisation energy and the total energy are completely smooth functions of the displacement coordinate, as should be expected since the amount of solute charge that is contained within the cavity does not change as a function of this deformation. Even with displacements as small as $\Delta x = 0.002$Å (inset of Figure 7), we observe no spurious wiggles –and certainly no discontinuities – in the energy. Addition of a nonelectrostatic term to the solvation energy will not change this situation since the cavity surface area is a continuous function of the nuclear

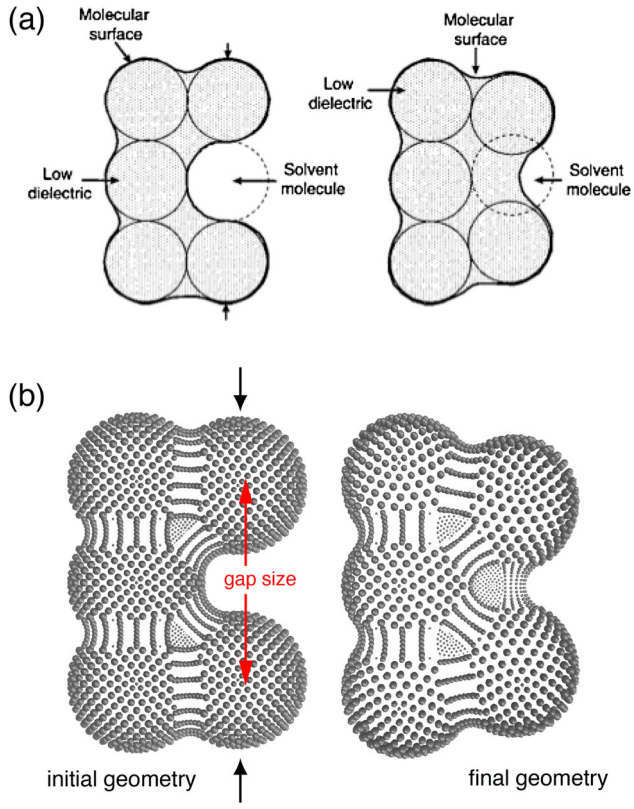

Figure 6. (a) Hypothetical example from Ref. [90] in which a small displacement of certain atomic spheres causes a large change in the SES. The 'low-dielectric' region is simply the interior of the SES. (b) SWIG discretisation grids for the initial and final geometries of this model problem, with arrows indicating how the atomic spheres are displaced to generate the final geometry. In (b), each grey ball is centred at a discretisation grid point, and the diameter of the ball is equal to $a_i^{1/2}$. The plane of the page divides the SES into two symmetry-equivalent halves and grid points lying behind that plane are omitted for visual clarity. Panel (a) is reproduced with permission from Ref. [90]; copyright 2001 John Wiley & Sons.

coordinates within our smooth SES construction. An example of such a nonelectrostatic term is presented in Section IV C.

Next we consider a realistic molecular example, namely, the torsional energy profile of the zwitterionic tautomer of the Gly-Gly dipeptide as a function of its backbone angle, ψ, with other internal coordinates held fixed. Representative structures along this coordinate are shown in Figure 8. The minimum-energy geometry corresponds to $\psi = 180^\circ$ and it should be noted that some of these structures are quite unrealistic (e.g. for $\psi \lesssim 60^\circ$), due to steric clash between two oxygen atoms that will be obvious from the energy profile. It is nevertheless interesting to examine the full domain of ψ, as this demonstrates that the cavity construction continues to function even in such cases. Moreover, in a QM/PCM context, one

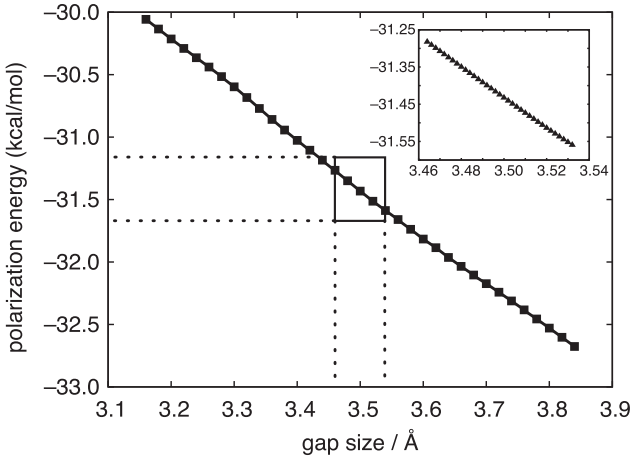

Figure 7. C-PCM polarisation energy for continuous deformation of the SES by adjusting the relative positions of two atomic spheres as indicated in Figure 6(b). The solute consists of classical atomic point charges and the medium is characterised by $\varepsilon = 78$. The inset is a close-up view of the region delineated in the box, in which the spacing between data points has been reduced from 0.020Å to 0.002Å.

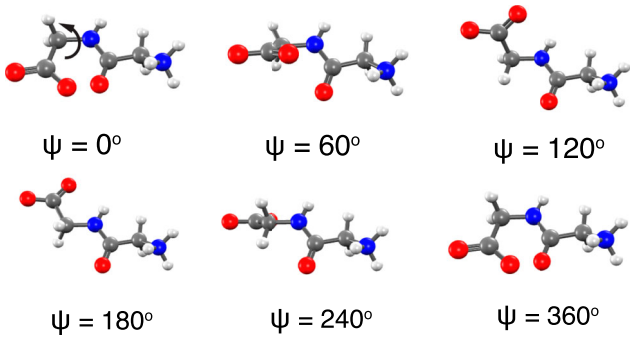

Figure 8. Structures of diglycine along a scan of the backbone torsion angle ψ, with other internal coordinates held fixed.

might want the ability to break bonds within the solute and thus the implicit solvent model, including the cavity construction algorithm, ideally ought to be able to handle this, as it can in our original SWIG algorithm [67]. (We will consider a bond-breaking example below.)

Figure 9 shows the Gly-Gly torsional energy profile computed at the B3LYP/6-31+G* level using C-PCM with $\varepsilon = 78.4$. The data points are very closely spaced ($\Delta\psi = 1^\circ$), yet the potential energy curves are completely smooth for both the 'r_{vdW}' and the '$r_{\mathrm{vdW}} + r_{\mathrm{probe}}$' versions of the SES. Energies obtained using SES(r_{vdW}) are noticeably offset from results obtained using the vdW construction even though the atomic radii are the same. However, the SES($r_{\mathrm{vdW}} + r_{\mathrm{probe}}$) surface (which uses radii $\eta + r_{\mathrm{probe}}$) affords results that are essentially identical to SAS results. The reason for this is intuitively clear from Figure 1: for the smaller radii, the crevices in the union-of-spheres surface are deeper,

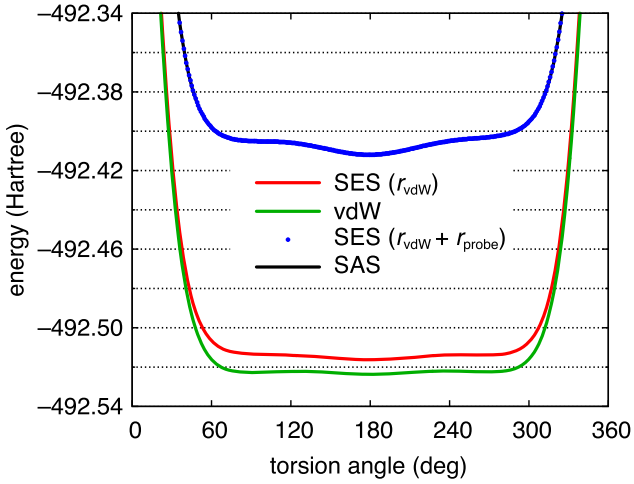

Figure 9. Absolute energy profiles of diglycine across the torsion angle ψ (see Figure 8), computed at the B3LYP/6-31+G* level with C-PCM and $\varepsilon = 78.4$, using various cavity definitions. For the SES, two different sets of radii are used. The traditional definition of the SES uses vdW radii and is indicated by SES(r_{vdW}); it is a vdW surface with cusps removed, as shown in Figure 1(a). Alternatively, SES($r_{\mathrm{vdW}} + r_{\mathrm{probe}}$) uses SAS radii, Equation (1), and corresponds to the SAS with cusps removed. With the larger radii $R_I = \eta + r_{\mathrm{probe}}$, energy profiles based on the SES and the SAS are essentially identical.

and thus the SES(r_{vdW}) construction modifies the vdW construction more so than the SES($r_{\mathrm{vdW}} + r_{\mathrm{probe}}$) construction modifies the SAS.

In fact, the $r_{\mathrm{vdW}} + r_{\mathrm{probe}}$ version of the SES modifies the SAS so little that even zooming in on the minimum-energy configuration, and setting $E(\psi = 180^\circ)$ equal to zero for all methods, we can discern virtually no difference between SES($r_{\mathrm{vdW}} + r_{\mathrm{probe}}$) and SAS results; see Figure 10. In the case of the traditional construction SES(r_{vdW}), the torsional profile is noticeably different as compared to that predicted using the vdW cavity, for the reason discussed above, but the important result is that the SES energy profiles are smooth. In the SES(r_{vdW}) results one can observe very small bumps in the potential energy curve, e.g. for $\psi \approx 270^\circ$, but these are not discontinuities. To demonstrate what genuine discontinuities look like in comparison, we performed a PCM calculation using the vdW cavity but discretised in a 'fixed' away, without the benefit of switching functions to ensure continuity. The vdW(fixed) energy profile in Figure 10 basically tracks the smooth vdW(SWIG) potential curve, but numerous and sizable discontinuities are evident. For vdW surfaces, we have previously documented the serious problems that such discontinuities cause, e.g. in geometry optimisations, vibrational frequency calculations, and molecular dynamics [66,67].

It is beyond the scope of this work to consider which of these cavity constructions is most accurate. In quantum

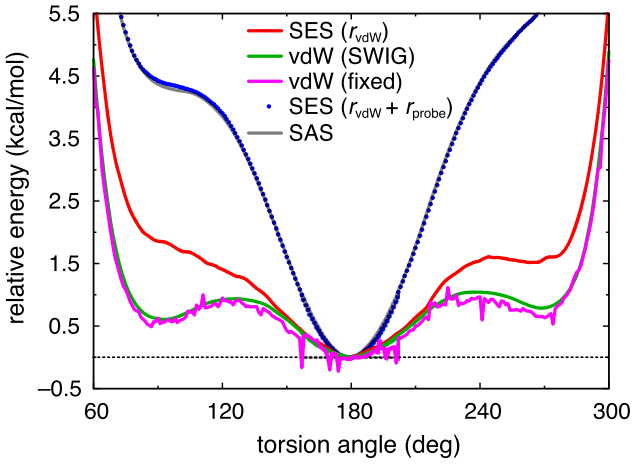

Figure 10. Relative energy profiles of diglycine across the torsion angle ψ (see Figure 8), computed at the B3LYP/6-31+G* level with C-PCM and $\varepsilon = 78.4$, using various cavity definitions. For the vdW surface, intrinsically-smooth SWIG results are shown along with a 'fixed' discretisation algorithm that does not employ a switching function, leading to discontinuities in the potential energy surface. All of the potential curves are set to zero at their respective minima except for the vdW(fixed) curve, which is set to zero at $\psi = 180^\circ$.

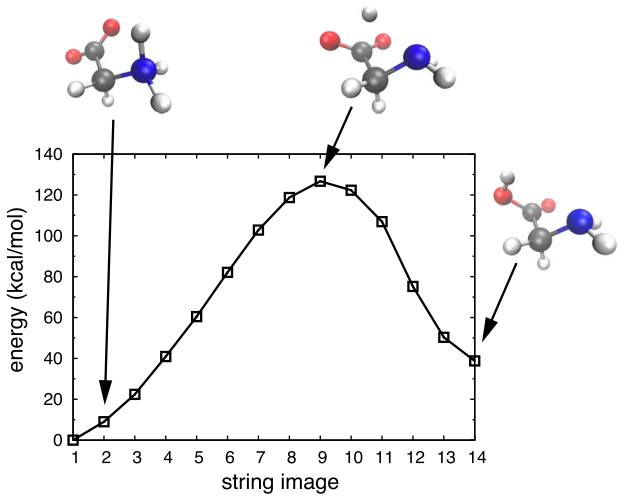

Figure 11. Energy profile for intramolecular proton transfer in glycine, computed using the frozen string method. Calculations were performed at the B3LYP/6-31+G* level using the SES in conjunction with C-PCM and $\varepsilon = 78.4$.

chemistry applications of PCMs, it is traditional to scale the Bondi radii by a factor of 1.2 [5], which we have not done here because such scaling is atypical in biomolecular applications. As mentioned above, our algorithm for surface construction appears to be competitive in cost with alternatives currently in use in the biomolecular simulation community [51].

For QM/PCM calculations, an important feature of the SWIG discretisation scheme is that the potential surface remains continuous even for chemical reactions. We have previously demonstrated this for the vdW-SWIG surface using the intramolecular proton transfer reaction in glycine [67], where the $NH_2CH_2CO(O)H$ tautomer that is the most stable geometry in the gas phase spontaneously forms the zwitterion $^+NH_3CH_2CO_2^-$ in water. For the present work, we used the freezing string algorithm [91] (with finite-difference gradients) to determine a pathway between these two isomers in aqueous solution, represented by C-PCM with $\varepsilon = 78$. A portion of this pathway is shown in Figure 11. Although the spacing between the images (nodes on the string) is large as compared to the very small spacing ($\Delta\psi = 1^\circ$) in the diglycine example, it is nevertheless clear from Figure 11 that the energy profile is smooth, despite the significant changes in bonding evident from the chemical structures that are shown.

C. Surface areas

Within the discretised approach, the SES molecular surface area is equal to the sum of all surface areas associate with atomic grid points (a_i^{atomic}, Equation (11)), toroidal grid points (a_i^{torus}, Equation (23)), and spherical re-entrant grid points ($a_i^{\text{spherical}}$, Equation (35)). As in our original SWIG implementation of the vdW surface [66,67], these discretised surface areas include a factor of the switching function, and are therefore smoothly attenuated to zero as $\mathbf{s}_i$ passes from the exterior to the interior of the cavity or *vice versa*. In Figure 12, we plot the total surface area afforded by several different cavity constructions, for the same diglycine torsional coordinate that was considered in Sectoin IV B and found to afford smooth energy profiles for SWIG-based cavity constructions.

In Figure 12(a), surface areas for the vdW(SWIG) and vdW(fixed) cavities are compared to those for SES-SWIG, using the same (unscaled Bondi) atomic radii in each case. Clearly and unsurprisingly, the vdW(fixed) construction exhibits discontinuous jumps on nearly every single step in the torsion angle, despite the very small step size of $\Delta\psi = 1^\circ$. These discontinuities are eliminated by the vdW(SWIG) construction, which predicts a slightly larger surface area as compared to the vdW(fixed) construction, but generally the former tracks the latter, without the discontinuities. The SES-SWIG construction results in a noticeably smaller surface area, as the deep, sharp cusps in the vdW surface are pushed out and smoothed. We must also note that although the SES-SWIG surface is provably smooth in the mathematical sense of possessing continuous derivatives, at a colloquial or intuitive level it is certainly 'less smooth'

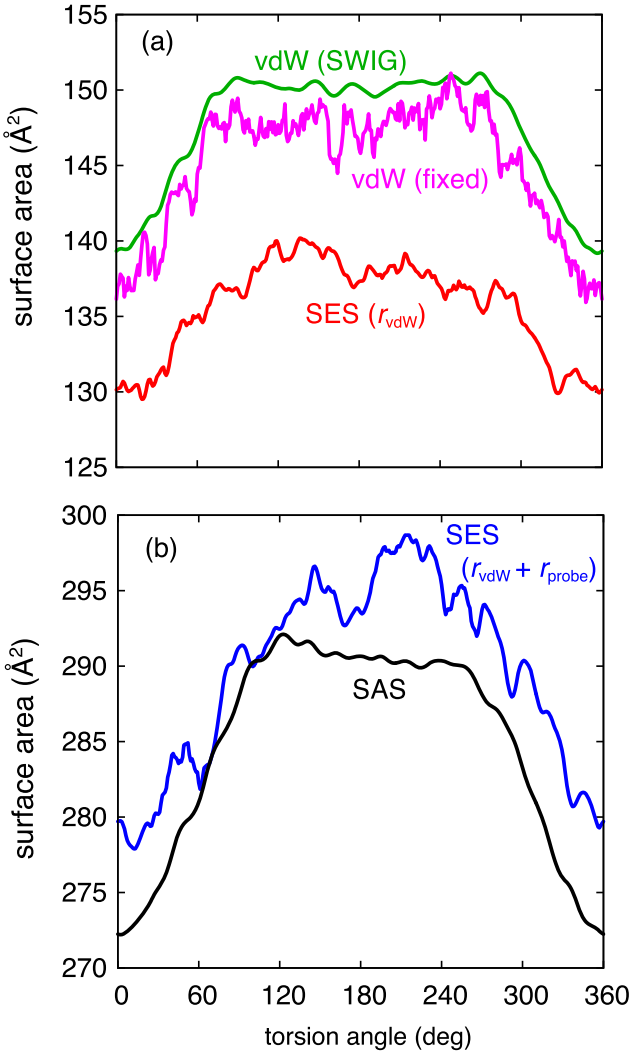

Figure 12. Surface area of diglycine along the torsion angle profile, computed using cavity surface definitions based on (a) Bondi's vdW radii or else (b) Bondi radii augmented by a 1.4Å probe radius. In (a), we compare surface areas for the vdW surface based on a primitive ('fixed') Lebedev discretisation with no switching function, versus those computed with the smooth SWIG approach. All cavities except the 'fixed' vdW one are constructed using the SWIG approach.

as compared to the vdW(SWIG) surface, in the sense of exhibiting more rapid oscillations in the surface area as a function of ψ.

Recall that the energy profiles as a function of ψ that are obtained from the vdW(SWIG) and SES-SWIG cavity constructions are somewhat different when Bondi radii are used (Figure 10), but are essentially identical when these atomic radii are augmented by the solvent probe radius. In light of this, we have also computed the surface area profiles using these augmented radii, which means a comparison of the SAS cavity and the SES($r_{vdW} + r_{probe}$) cavity, which is shown in Figure 12(b). As expected, the difference between the two surface areas is generally smaller than the difference between the vdW and SES(r_{vdW}) surface areas, although the SES($r_{vdW} + r_{probe}$) surface area continues to exhibit more rapid (albeit smooth) oscillations.

The fact that the SES($r_{vdW} + r_{probe}$) surface exhibits such oscillations leads us to suspect that these are simply an intrinsic feature of the discretised SES; convergence tests with respect to the number of discretisation grid points seem to bear this out. In Figure 13(a) we vary the number of Lebedev points used to discretise each spherical surface element, using a fixed 20 × 20 grid for the toroidal elements. Oscillations in the total surface area persist, even though the total change in the surface area is small, as the grid is switched between $N = 110$, 302, and 590 points per spherical facet. In Figure 13(b), we fix the spherical grid at 110 points and vary the $N \times N$ re-entrant grid (see Table 2) between $N = 4$, 10, 14, and 20. These variations have a somewhat larger effect on

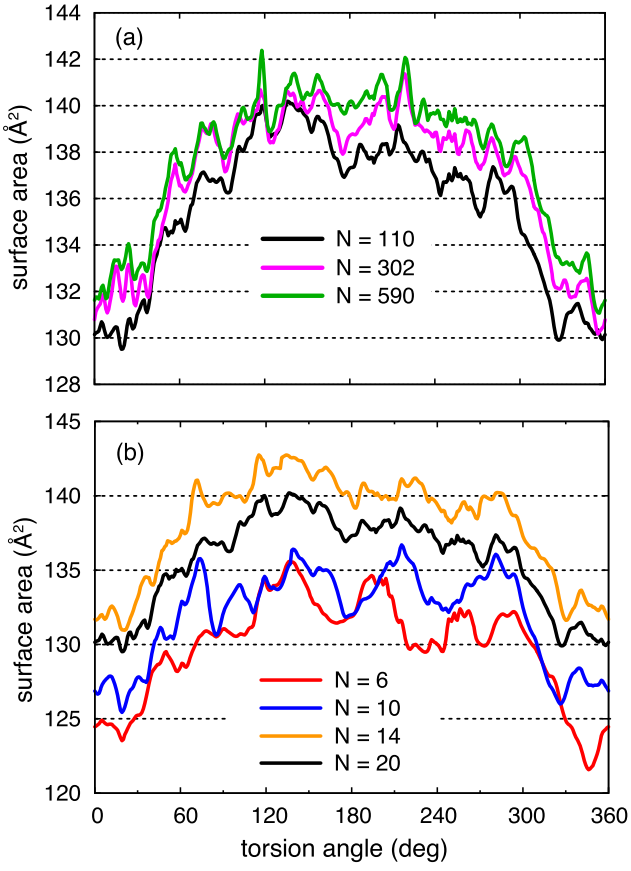

Figure 13. SES surface area for diglycine along its torsion angle profile, as a function of the number of surface discretisation points: (a) varying the number of grid points per spherical surface element, using a fixed 20 × 20 grid to discretise the toroidal elements; and (b) varying the toroidal grid for a fixed value of 110 points per spherical element. The black curves in (a) and (b) are the same data, for a 20 × 20 grid for the re-entrant surface elements and 110 points per atomic sphere.

the overall surface area as compared to changes in the spherical grid, and the fluctuations remain.

QM-based implicit solvation models often contain a non-electrostatic (or 'non-polar') term proportional to the cavity surface area [92–94], intended to capture van der Waals and Pauli repulsion interactions, and we wish to examine whether fluctuations in surface area of the magnitude documented above are important or problematic in this context. To do this, we consider a slightly more sophisticated model for the non-electrostatic free energy,

$$\Delta G_{\text{nonels}} = \sum_{I}^{\text{atoms}} \sigma_I A_I, \tag{38}$$

parameterised in terms of 'solvent-exposed' atomic surface areas A_I (i.e. the contribution to total surface area arising from atom I), with parameters σ_I having dimensions of surface tension. In the MM community, models based on Equation (38) are known as *solvent-accessible surface area* (SASA) models [11,95], but this functional form is also used in some QM solvation models including the popular SM*x* models [96, 97].

We are not aware of any non-electrostatic model that is parameterised for use with the SES, and to do so the re-entrant surface elements would need to be assigned to particular atoms. This is feasible but is beyond the scope of the present work. Instead, we consider non-electrostatic models parameterised for use with the vdW surface, and compare the vdW(SWIG) and vdW(fixed) cavity constructions as the latter obviously exhibits much larger fluctuations, e.g. as a function of the diglycine torsional coordinate. Figure 14 shows the non-electrostatic energy profile obtained along this coordinate, using the aforementioned cavity constructions in conjunction with the 'AGBNP' non-electrostatic model of Ref. [98]. (For this purpose we use the atomic radii suggested in Ref. [98], which differ from Bondi's values, to construct the cavity.) Clearly, the sharp discontinuities in the total surface area (and, by extension, in the individual atomic surface areas as well) exhibited by the vdW(fixed) construction manifest directly as discontinuities in the SASA non-electrostatic energy as a function of the dihedral angle. The vdW(SWIG) construction smooths this out. The same behaviour is observed with an alternative parameterisation of the non-electrostatic energy [99], although in this case the total non-electrostatic contribution is < 1 kcal/mol and the fluctuations correspondingly smaller. Even given the larger and highly fluxional values of the AGBNP-vdW(fixed) non-electrostatic energy, however, we note that the changes in energy from one step to the next are rather small. Given that the (smooth) oscillations in the SES surface area are smaller in magnitude that the (discontinuous) oscillations in the vdW(fixed) surface area, we expect that any reasonable parameterisation of a SASA model for use with the SES would likely exhibit fluctuations in the energy that are small compared to those observed for AGBNP-vdW(fixed). We conclude that the (apparently intrinsic) fluctuations in the discretised SES surface area seem unlikely to be problematic in practice.

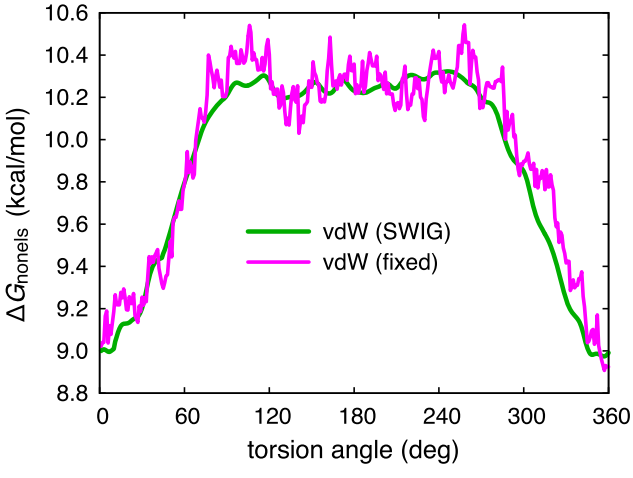

Figure 14. Non-electrostatic contribution to the solvation energy as predicted by the AGBNP model [98], which depends on the exposed atomic surface areas (Equation (38)). The vdW cavity construction is used, but with atomic radii as suggested in Ref. [98] rather than Bondi radii.

V. Summary

We have presented a method for computing Connolly's solvent-excluded surface, through a generalisation of the switching/Gaussian method introduced previously for discretisation of other types of solute/continuum boundaries [66,67]. The new approach, SES-SWIG, affords a discretisation of the surface that is continuous and smooth with respect to displacements of the atomic coordinates. As such, it is appropriate for use in the numerical surface integrals that appear in boundary-element formulations of continuum electrostatics, including polarisable continuum models.

Acknowledgements

A.W.L. acknowledges a Presidential Fellowship from the Graduate School of The Ohio State University.

Disclosure statement

J.M.H. serves on the Board of Directors of Q-Chem Inc.

Funding

This work was supported by the National Science Foundation, Division of Chemistry [grant numbers CHE-0748448, CHE-1300603, and CHE-1665322]. Calculations were performed at the Ohio Supercomputer Center under project PAA0003 [100].

References

[1] A. Bondi, J. Phys. Chem. **68**, 441 (1964).
[2] R.S. Rowland and R. Taylor, J. Phys. Chem. **100**, 7384 (1996).
[3] R. Bonaccorsi, P. Palla, and J. Tomasi, J. Am. Chem. Soc. **106**, 1945 (1984).
[4] A. Klamt and G. Schüürmann, J. Chem. Soc. Perkin Trans. **2**, 799 (1993).
[5] J.M. Herbert and A.W. Lange, in *Many-Body Effects and Electrostatics in Biomolecules*, edited by Q. Cui, P. Ren, and M. Meuwly (CRC Press, Boca Raton, FL, 2016), Chap. 11, pp. 363–416.
[6] D.H. Brookes and T. Head-Gordon, J. Phys. Chem. Lett. **6**, 2938 (2015).
[7] B. Lee and F.M. Richards, J. Mol. Biol. **55**, 379 (1971).
[8] S. Sridharan, A. Nicholls, and K. Sharp, J. Comput. Chem. **16**, 1038 (1995).
[9] D.-S. Kim, C.-I. Won, and J. Bhak, J. Biomol. Struct. Dyn. **28**, 277 (2010).
[10] S. Wei, C.L. Brooks, III, and A.T. Frank, J. Comput. Chem. **38**, 1270 (2017).
[11] J. Gasteiger and T. Engel, editors, *Chemoinformatics: A Textbook* (Wiley-VCH, Weinheim, 2003).
[12] J. Tomasi, B. Mennucci, and R. Cammi, Chem. Rev. **105**, 2999 (2005).
[13] J. Tomasi, B. Mennucci, and E. Cancès, J. Mol. Struct. (Theochem) **464**, 211 (1999).
[14] D.M. Chipman, J. Chem. Phys. **112**, 5558 (2000).
[15] D.M. Chipman, Theor. Chem. Acc. **107**, 80 (2002).
[16] H. Tjong and H.-X. Zhou, J. Chem. Theory Comput. **4**, 507 (2008).
[17] H.-X. Zhou, S. Qin, and H. Tjong, Annu. Rep. Comput. Chem. **4**, 67 (2008).
[18] X. Pang and H.-X. Zhou, Commun. Comput. Phys. **13**, 1 (2013).
[19] S. Decherchi, J. Colmenares, C.E. Catalano, M. Spagnuolo, E. Alexov, and W. Rocchia, Commun. Comput. Phys. **13**, 61 (2013).
[20] A.V. Onufriev and B. Aguilar, J. Theor. Comput. Chem. **13**, 1440006 (2014).
[21] F.M. Richards, Annu. Rev. Biophys. Bio. **6**, 151 (1977).
[22] M.L. Connolly, Science **221**, 709 (1983).
[23] M.L. Connolly, J. Appl. Cryst. **16**, 548 (1983).
[24] T.J. Richmond, J. Mol. Biol. **178**, 63 (1984).
[25] R.J. Zauhar and R.S. Morgan, J. Comput. Chem. **11**, 603 (1990).
[26] F. Eisenhaber and P. Argos, J. Comput. Chem. **14**, 1272 (1993).
[27] J.L.P. Ahuir and E. Silla, J. Comput. Chem. **11**, 1047 (1990).
[28] E. Silla, I. Tuñon, and J.L.P. Ahuir, J. Comput. Chem. **12**, 1077 (1991).
[29] J.L.P. Ahuir, E. Silla, and I. Tuñon, J. Comput. Chem. **15**, 1127 (1994).
[30] A. Varshney, F.P. Brooks, Jr., and W.V. Wright, IEEE Comp. Graph. Appl. **14**, 19 (1994).
[31] R.J. Zauhar, J. Comput.-Aided Mol. Des. **9**, 149 (1995).
[32] T. You and D. Bashford, J. Comput. Chem. **16**, 743 (1995).
[33] M.F. Sanner, A.J. Olson, and J.-C. Spehner, Biopolymers **38**, 305 (1996).
[34] C. Bajaj, H.Y. Lee, R. Merkert, and V. Pascucui, NURBS based B-rep models for macromolecules and their properties, in *Proceedings of the Fourth ACM Symposium on Solid Modeling and Applications*, SMA '97 (ACM, New York, 1997), pp. 217–228.
[35] J. Liang, H. Edelsbrunner, P. Fu, P.V. Sudhakar, and S. Subramaniam, Proteins **33**, 1 (1998).
[36] W. Rocchia, S. Sridharan, A. Nicholls, E. Alexov, A. Chiabrera, and B. Honig, J. Comput. Chem. **23**, 128 (2002).
[37] C. Bystroff, Protein Eng. Des. Sel. **15**, 959 (2002).
[38] J. Buša, J. Dzurina, E. Hayryanm, S. Hayryan, C.-K. Hu, J. Plávka, I. Pokorný, J. Skrivánek, and M.-C. Wu, Comput. Phys. Comm. **165**, 59 (2005).
[39] T. Can, C.-I. Chen, and Y.-F. Wang, J. Mol. Graph. Model. **25**, 442 (2006).
[40] J.P. Bardhan, M.D. Altman, D.J. Willis, S.M. Lippow, B. Tidor, and J.K. White, J. Chem. Phys. **127**, 014701 (2007).
[41] J. Ryu, R. Park, and D.-S. Kim, Comput. Aided Des. **39**, 1042 (2007).
[42] D. Xu and Y. Zhang, PLoS ONE **4**, e8140 (2009).
[43] H. Harbrecht and M. Randrianarivony, Computing **92**, 335 (2011).
[44] K.V. Klenin, F. Tristam, T. Strunk, and W. Wenzel, J. Comput. Chem. **32**, 2647 (2011).
[45] S. Decherchi and W. Rocchia, PLoS ONE **8**, e59744 (2013).
[46] B. Liu, B. Wang, R. Zhao, Y. Tong, and G.-W. Wei, J. Comput. Chem. **38**, 446 (2017).
[47] M.L. Connolly, J. Mol. Graphics **11**, 139 (1993).
[48] B. Huang and M. Schroeder, BMC Struct. Biol. **6**, 19 (2006).
[49] S.-H. Wang, Y.-T. Wu, S.-C. Kuo, and J. Yu, J. Chem. Inf. Model. **53**, 2181 (2013).
[50] N.A. Baker, D. Sept, M.J. Holst, and J.A. McCammon, IBM J. Res. Dev. **45**, 427 (2001).
[51] Q. Cai, X. Ye, J. Wang, and R. Luo, J. Chem. Theory Comput. **7**, 3608 (2011).
[52] D.D. Nguyen, B. Wang, and G.-W. Wei, J. Comput. Chem. **38**, 941 (2017).
[53] W. Im, D. Beglov, and B. Roux, Comput. Phys. Commun. **111**, 59 (1998).
[54] B. Lu, D. Zhang, and J.A. McCammon, J. Chem. Phys. **122**, 214102 (2005).
[55] J. Wang, C. Tan, Y.-H. Tan, Q. Lu, and R. Luo, Commun. Comput. Phys. **3**, 1010 (2008).
[56] J. Wang, Q. Cai, Y. Xiang, and R. Luo, J. Chem. Theory Comput. **8**, 2741 (2012).
[57] Q. Lu and R. Luo, J. Chem. Phys. **119**, 11035 (2003).
[58] J. Chocholoušová and M. Feig, J. Comput. Chem. **27**, 719 (2006).
[59] A.V. Onufriev and D.A. Case, Annu. Rev. Biophys. **48**, 275 (2019).

[60] M.S. Lee, F.R. Salsbury, Jr., and C.L. Brooks, III, J. Chem. Phys. **116**, 10606 (2002).
[61] M.S. Lee, M. Feig, and F.R. Salsbury, Jr., J. Comput. Chem. **24**, 1348 (2003).
[62] D.M. York and M. Karplus, J. Phys. Chem. A **103**, 11060 (1999).
[63] C.S. Pomelli, J. Comput. Chem. **25**, 1532 (2004).
[64] H. Li and J.H. Jensen, J. Comput. Chem. **25**, 1449 (2004).
[65] P. Su and H. Li, J. Chem. Phys. **130**, 074109 (2009).
[66] A.W. Lange and J.M. Herbert, J. Phys. Chem. Lett. **1**, 556 (2010).
[67] A.W. Lange and J.M. Herbert, J. Chem. Phys. **133**, 244111 (2010).
[68] A.W. Lange and J.M. Herbert, J. Chem. Phys. **134**, 117102 (2011).
[69] A.W. Lange and J.M. Herbert, J. Chem. Phys. **134**, 204110 (2011).
[70] A.W. Lange and J.M. Herbert, Chem. Phys. Lett. **509**, 77 (2011).
[71] B. Mennucci, WIREs Comput. Mol. Sci. **2**, 386 (2012).
[72] M.R. Provorse, T. Peev, C. Xiong, and C.M. Isborn, J. Phys. Chem. B **120**, 12148 (2016).
[73] M.P. Coons and J.M. Herbert, J. Chem. Phys. **148**, 222834 (2018).
[74] V.I. Lebedev, Zh. vy chisl, Mat. Mat. Fiz. **16**, 293 (1975).
[75] V.I. Lebedev, USSR Comp. Math. Math+ **15**, 44 (1975).
[76] L. Xiao, Q. Cai, X. Ye, J. Wang, and R. Luo, J. Chem. Phys. **139**, 094106 (2013).
[77] A.W. Lange and J.M. Herbert, J. Chem. Theory Comput. **8**, 1999 (2012).
[78] A.W. Lange and J.M. Herbert, J. Chem. Theory Comput. **8**, 4381 (2012).
[79] E.W. Weisstein, *CRC Encyclopedia of Mathematics*, 2nd ed. (Chapman and Hall/CRC, Boca Raton, FL, 2003).
[80] E. Abbena, S. Salamon, and A. Gray, *Modern Differential Geometry of Curves and Surfaces with Mathematica*, 3rd ed. (Chapman and Hall/CRC, Boca Raton, FL, 2006).
[81] B.A. Gregersen and D.M. York, J. Chem. Phys. **122**, 194110 (2005).
[82] M. Born, Z. Phys. **1**, 45 (1920).
[83] S. Miertuš, E. Scrocco, and J. Tomasi, Chem. Phys. **55**, 117 (1981).
[84] S. Miertuš and J. Tomasi, Chem. Phys. **65**, 239 (1982).
[85] E.O. Purisima and S.H. Nilar, J. Comput. Chem. **16**, 681 (1995).
[86] A.I. Krylov and P.M.W. Gill, WIREs Comput. Mol. Sci. **3**, 317 (2013).
[87] Y. Shao, Z. Gan, E. Epifanovsky, A.T.B. Gilbert, M. Wormit, J. Kussmann, A.W. Lange, A. Behn, J. Deng, X. Feng, D. Ghosh, M. Goldey, P.R. Horn, L.D. Jacobson, I. Kaliman, R.Z. Khaliullin, T. Kuś, A. Landau, J. Liu, E.I. Proynov, Y.M. Rhee, R.M. Richard, M.A. Rohrdanz, R.P. Steele, E.J. Sundstrom, H. Lee Woodcock, III, P.M. Zimmerman, D. Zuev, B. Albrecht, E. Alguire, B. Austin, G.J.O. Beran, Y.A. Bernard, E. Berquist, K. Brandhorst, K.B. Bravaya, S.T. Brown, D. Casanova, C.-M. Chang, Y. Chen, S.H. Chien, K.D. Closser, D.L. Crittenden, M. Diedenhofen, R.A. DiStasio, Jr., H. Do, A.D. Dutoi, R.G. Edgar, S. Fatehi, L. Fusti-Molnar, A. Ghysels, A. Golubeva-Zadorozhnaya, J. Gomes, M.W.D. Hanson-Heine, P.H.P. Harbach, A.W. Hauser, E.G. Hohenstein, Z.C. Holden, T.-C. Jagau, H. Ji, B. Kaduk, K. Khistyaev, J. Kim, J. Kim, R.A. King, P. Klunzinger, D. Kosenkov, T. Kowalczyk, C.M. Krauter, K.U. Lao, A.D. Laurent, K.V. Lawler, S.V. Levchenko, C.Y. Lin, F. Liu, E. Livshits, R.C. Lochan, A. Luenser, P. Manohar, S.F. Manzer, S.-P. Mao, N. Mardirossian, A.V. Marenich, S.A. Maurer, N.J. Mayhall, E. Neuscamman, C. Melania Oana, R. Olivares-Amaya, D.P. O'Neill, J.A. Parkhill, T.M. Perrine, R. Peverati, A. Prociuk, D.R. Rehn, E. Rosta, N.J. Russ, S.M. Sharada, S. Sharma, D.W. Small, A. Sodt, T. Stein, D. Stück, Y.-C. Su, A.J.W. Thom, T. Tsuchimochi, V. Vanovschi, L. Vogt, O. Vydrov, T. Wang, M.A. Watson, J. Wenzel, A. White, C.F. Williams, J. Yang, S. Yeganeh, S.R. Yost, Z.-Q. You, I.Y. Zhang, X. Zhang, Y. Zhao, B.R. Brooks, G.K.L. Chan, D.M. Chipman, C.J. Cramer, W.A. Goddard, III, M.S. Gordon, W.J. Hehre, A. Klamt, H.F. Schaefer, III, M.W. Schmidt, C. David Sherrill, D.G. Truhlar, A. Warshel, X. Xu, A. Aspuru-Guzik, R. Baer, A.T. Bell, N.A. Besley, J.-D. Chai, A. Dreuw, B.D. Dunietz, T.R. Furlani, S.R. Gwaltney, C.-P. Hsu, Y. Jung, J. Kong, D.S. Lambrecht, W.Z. Liang, C. Ochsenfeld, V.A. Rassolov, L.V. Slipchenko, J.E. Subotnik, T. Van Voorhis, J.M. Herbert, A.I. Krylov, P.M.W. Gill, and M. Head-Gordon, Mol. Phys. **113**, 184 (2015).
[88] E. Cancès and B. Mennucci, J. Math. Chem. **23**, 309 (1998).
[89] D.M. Chipman, J. Chem. Phys. **120**, 5566 (2004).
[90] J.A. Grant, B.T. Pickup, and A. Nicholls, J. Comput. Chem. **22**, 608 (2001).
[91] A. Behn, P.M. Zimmerman, A.T. Bell, and M. Head-Gordon, J. Chem. Phys. **135**, 224108 (2011).
[92] D.A. Scherlis, J.-L. Fattebert, F. Gygi, M. Cococcioni, and N. Marzari, J. Chem. Phys. **124**, 074103 (2006).
[93] O. Andreussi, I. Dabo, and N. Marzari, J. Chem. Phys. **136**, 064102 (2012).
[94] M. Sinstein, C. Scheurer, S. Matera, V. Blum, K. Reuter, and H. Oberhofer, J. Chem. Theory Comput.**13**, 5582 (2017).
[95] J. Kleinjung and F. Fraternali, Curr. Opin. Struc. Biol. **25**, 126 (2014).
[96] C.J. Cramer and D.G. Truhlar, Acc. Chem. Res. **41**, 760 (2008).
[97] J. Liu, C.P. Kelly, A.C. Goren, A.V. Marenich, C.J. Cramer, D.G. Truhlar, and C.-G. Zhan, J. Chem. Theory Comput. **6**, 1109 (2010).
[98] E. Gallicchio and R.M. Levy, J. Comput. Chem. **25**, 479 (2004).
[99] D. Eisenberg and A.D. McLachlan, Nature **319**, 199 (1986).
[100] Ohio Supercomputer Center http://osc.edu/ark:/19495/f5s1ph73.